4 Experimental outline

Section 3 presented the fundamentals of a technique allowing the profiles of reflective surfaces to be measured. In the following pages the experimental outline used to obtain the measurements presented in Sections 6 and 7 of the present work is described.

This section is divided into three parts. In the first one the setup implemented in the laboratory will be presented. The second part describes in full the whole data processing procedure carried out from obtaining experimental data to finding the parameters that describe the final reconstruction of the surface. These two subsections start with a general description of the elements or processes that will later be presented in detail, in order to provide an overview of what will be presented next. In the third subsection the accuracy achieved under our experimental conditions is studied.

4.1. Experimental setup

A general overview of the laboratory equipment and the experimental arrangement implemented is shown in Fig. 4.1.1 and will be described at length below. As a general overview of the setup, an intensity source power supply feeds a laser diode coupled to an optical fiber. This allows a precisely located small spot (4μm wide) to be used as a point light source, which diverges towards a pellicle beam-splitter. Fifty percent of the light intensity continues to diverge until it impinges on the surface being tested, which reflects the incident-diverging beam. After crossing the beam-splitter again, this reflected beam of light passes through the Ronchi ruling, and a shadow pattern of the lines on the ruling is produced. A CCD camera registers the slopes of the reflected light beam, with the superimposed information of the period of the lines on the Ronchi ruling; this registered information will hereafter be called a ronchigram. The ronchigram is recorded via a frame-grabber placed in a 80486 PC, connected to an RGB monitor. Further data processing will be carried out with a Pentium PC, connected to the former via a parallel data link in order to achieve fast data transmission. The plane where the Ronchi ruling is placed is motorized in order to be displaced along two orthogonal directions in the plane, coincident with the defined X and Y axes in Fig. 4.1.1, through encoder motors, and it can also be rotated around the Z axis via a stepping motor. These motors are controlled using a third computer, in this case a PS2, connected via a serial link to the 80486 PC, allowing remote control of the position and orientation of the Ronchi test. As the 80486 PC has a link to the motor control unit (PS2), data processing unit (Pentium PC) and data acquisition unit (frame grabber plus RGB monitor), it acts as the master control unit of the experimental setup. Further details on each of the abovementioned elements are provided next.

4.1.1.- Light source

Certain trials were made prior to the final selection of the light source used, which was required to be as close to a point as possible, and with an easy-to-measure position. Our first attempts involved the usual solution in such cases, that is, a HeNe laser beam spatially filtered using a 20x objective and a pinhole. However, such arrangements were impractical, as the surface where the experiment was mounted could not be vibration-isolated; this usually brought about misalignments of the source.

Fig.4.1.1: Experimental setup: General overview

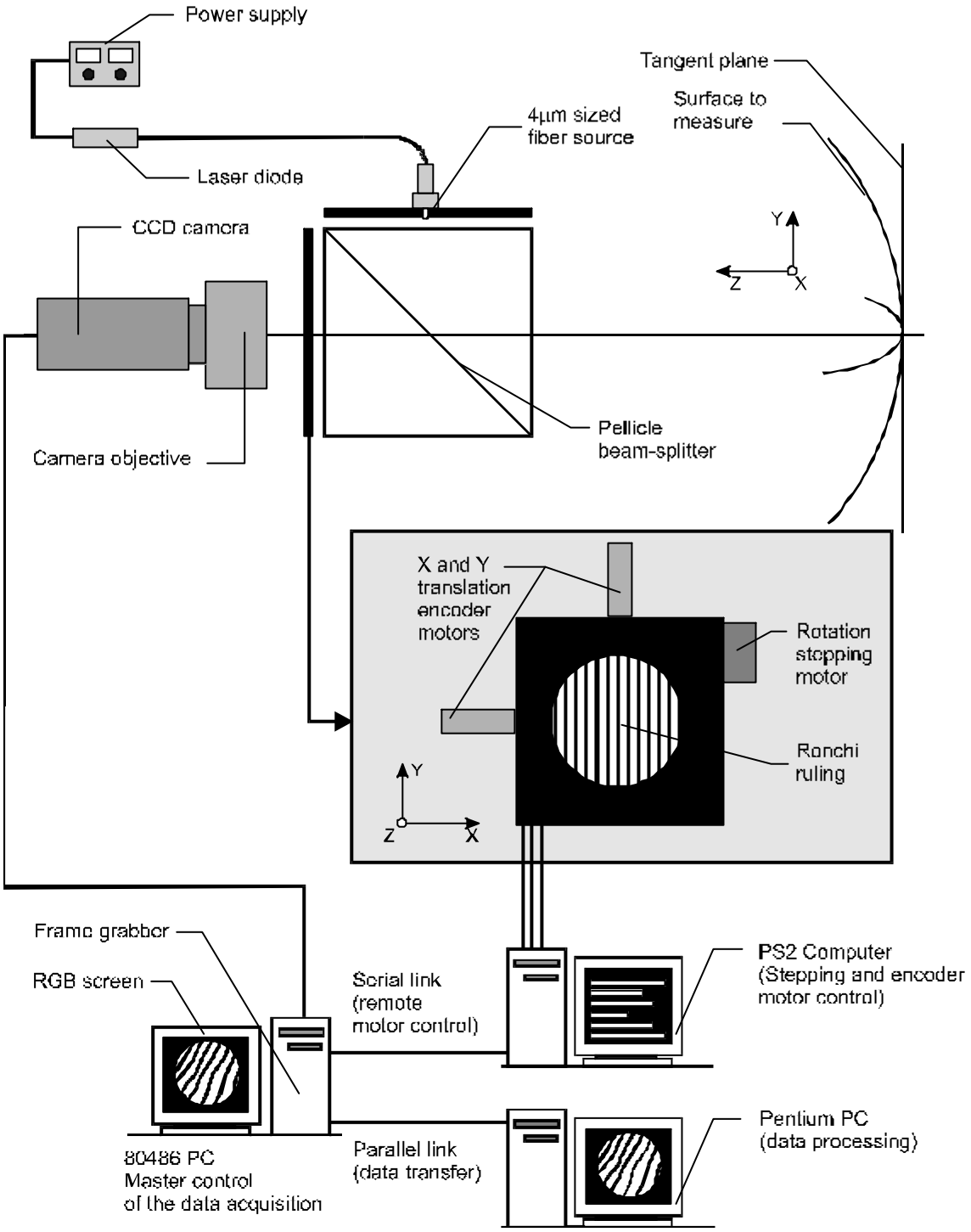

A second arrangement was then implemented, using a HeNe laser beam which passed through a rotating diffuser. The spot on the diffuser provided a target for a 50x microscope objective which formed a point image a few millimeters away from the objective surface. The described setup is presented in Fig. 4.1.2.

This second setup for the light source solved the misalignment problems of arrangements using a pinhole, but also entailed a new set of problems. First of all, the use of a diffuser introduced speckle effects in the ronchigrams, which needed to be removed by rotating the diffuser and averaging of the measured data. However, the main drawback of this kind of light source was the impossibility of accurately locating the position of the point light source, which is a key data item needed to calculate the local normals to the surface.

All these problems led us to consider an alternative light source when designing the final experimental setup. Our requirements of a very small light source that is easy to handle and to position were fulfilled by an FC connectorized visible laser diode module, from Laser Technology, S.L., model LT635/1-4-1FC/PC, with a wavelength of 635nm and an output power of 3mW. This laser diode is coupled to an optical fiber ending in a 4μm wide head, which provides us with the ease of fiber positioning that we required. An intensity power supply yielding up to 100mA was designed and built in order to feed the laser diode.

Fig.4.1.2.-Second arrangement for the light source design (see text).

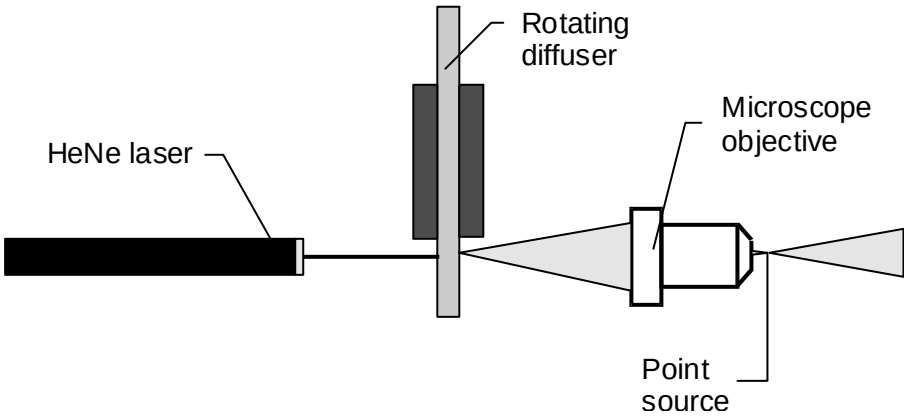

4.1.2.- Pellicle beam-splitter

Once the light leaves the optical fiber, the wavefront is divided by a 100mm diameter pellicle beam-splitter, in order to direct the light along an axis containing the

surface being tested and the Ronchi ruling. This axis will hereafter be called the Z axis. Its origin will be considered on the vertex of the surface, with its positive values increasing in the direction of the Ronchi ruling (Fig. 4.1.1). X and Y axes are defined consistently in the directions shown in Fig. 4.1.1.

A pellicle beam-splitter was chosen in order to avoid the effects introduced by beam-splitter cubes or plates. Both types of beam-splitters involve glass substrates which cause deformations in the shape of the wavefront hitting the surface, which will no longer be spherical, and the reflected wavefront on its way to the Ronchi ruling. As one of the key data-processing steps needed in order to measure the topography of a surface is a ray tracing procedure from the Ronchi plane to the tested surface, using a pellicle beam-splitter means that the rays propagate as straight lines from one element to the other. If a glass cube beam-splitter was used, light would find different refractive indexes and surfaces in its path and would unnecessarily complicate the calculation of the ray propagation from the Ronchi plane to the surface. Furthermore, in cube or plate beam-splitters, additional artifacts caused either by internal reflections on their surfaces or by the presence of possible unevenness or imperfections in the glass, might distort the wavefront to some extent. These effects led us to prefer a pellicle beam-splitter in our setup.

However, a pellicle beam-splitter is a very fragile piece of equipment, which needs to be properly mounted. An aluminum cube with a 99mm edge was designed, with its dimensions mechanically ensured up to 0.01mm. In order to provide a steady reference plane from which to make measurements, metal was only removed from half of the cube (from the main diagonal to one of the opposite vertices). 50mm diameter cylindrical holes at the center of the remaining surfaces ensured that light could travel across the cube (see Fig. 4.1.3).

4.1.3.- Surface being tested

The light has thus finally been directed towards the surface to be tested, along the Z axis. In our setup, the plane tangent to the surface at its vertex has been arranged to stay vertical (parallel to the XY plane). The mount of the surface is interchangeable in order to accept a range of surface diameters. The mount is allowed to rotate around the Z axis in 30° steps.

Fig. 4.1.3: Cube used as beam-splitter mount; (a) Seen from the source (YZ plane); an equivalent view may be obtained from the surface (XY plane); (b) Seen from upside (XZ plane).

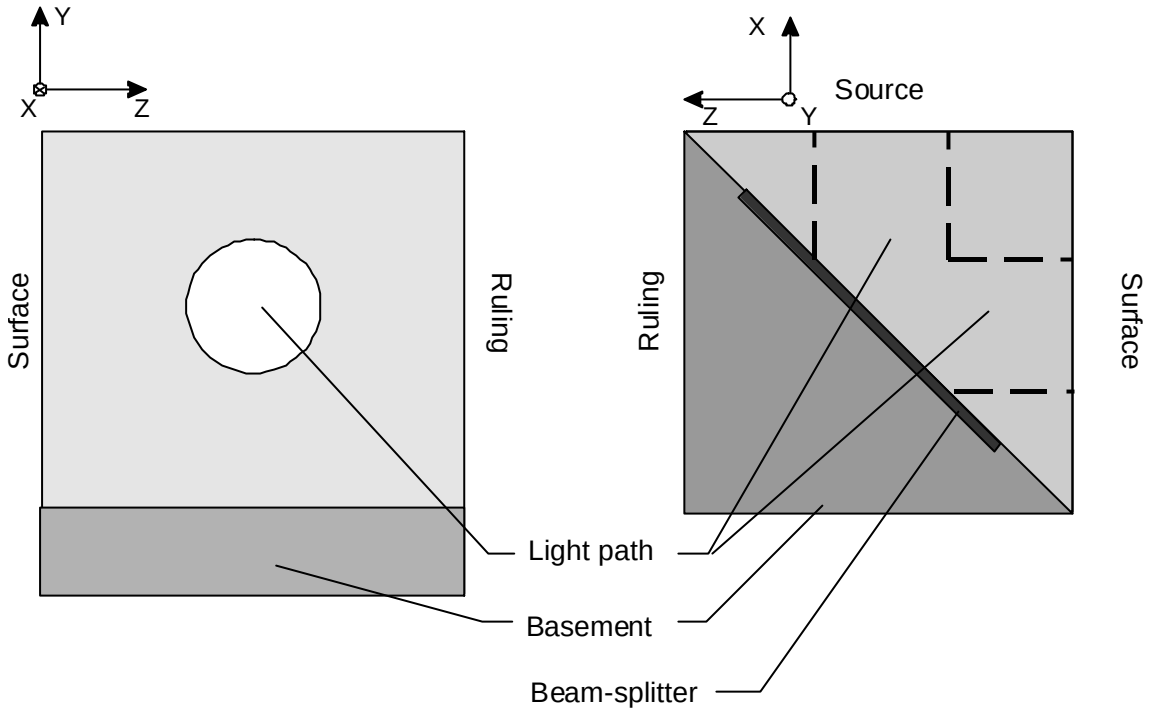

The surface mount is placed on a 1200mm long bench consisting of an inverted U-shaped iron beam weighing around 15kg. The cube mounting the pellicle beam-splitter, the Ronchi ruling and the CCD camera are firmly placed on this beam. A pair of iron bars are used as rails for a mobile platform, which will carry the mount of the surface being tested. The position of the platform along the Z axis is accurately measured via a Mitutoyo© magnetic ruler with 0.01mm resolution and 500mm maximum distance range. In order to measure the distance from the vertex of the surface to the cube surface, the outer limit of the surface mount is placed in contact with the cube mounting the beam-splitter, and the additional depth up to the vertex of the surface, including the lens sagitta, is then measured via a Mitutoyo© positioner, also with 0.01mm resolution. Two Oriel© 16061 positioning stages, together with a 15mm deep Oriel© positioner, allow the mount to move along the Y and X axis in order to adjust the centering and positioning of the sample better.

The surfaces being tested are all concave surfaces of ophthalmic lenses. This led to the measurement of spherical and toroidal surfaces, although some other surfaces used in the ophthalmic industry may have been also measured (for instance, the aspherical surfaces present in the moulds used in organic lens fabrication). Detailed information on sample trial will be provided along Sections 6.1 and 7.1. Because

ophthalmic lenses have two optically active surfaces, the convex surface of the lens needed to be made optically inactive, in order for it not to disturb the results from the concave one. In our setup, this was achieved through grinding this surface and painting it with matt black paint. A more elegant solution would be to place the plane tangent to the lens vertex horizontally (instead of vertically), and then to fill the gap from the surface to the mount with some index-matched liquid in order to suitably alter the amount of energy reflected. However, this approach would have meant major alterations in our setup, which were left for future work, once the abilities of the technique had been tested.

4.1.4.- The Ronchi ruling: position and movement

Once the light coming from the point source has hit the surface, the altered wavefront again travels through the pellicle beam-splitter and finally arrives at the Ronchi ruling. It is mounted on an Oriel© 13045 rotating mount, so the orientation of the lines may be modified at will. The mount incorporates a scale so rotations up to 0.1° may be measured.

Due to the importance of the position and orientation of the ruling, which will be used to improve the sampling of the wavefront (see Section 5.3), displacements along X and Y axes were motorized using two Oriel Mike© 18218 encoders which push one Oriel© 16061 positioning stage each. This allowed a theoretical limit to the displacements of 0.1μm to be implemented, though this was never needed in our experiments, and ensured full repeatability and control of the ruling displacements. Their maximum allowed excursion was around 10mm. An additional stepper motor (Fuji Electrochemical stepper motor SM55, with 3.5 arcminutes resolution) was added in the rotation axis of the rotating Oriel© 13045 mount, which allowed a reliable and repetitive motorized rotation of the Ronchi ruling.

The Oriel Mike© motors were controlled by means of a specially designed interface card, and the stepper motor by means of a common PPI card. Both cards were placed in a PS2 computer. The control algorithms for both the encoders and the stepping motor were programmed in C language on the same computer. This computer was also connected via its serial port to a 80486 PC, which controlled the frame-grabber connected to the CCD camera. This serial communication allowed remote control of the motors from the computer containing the frame-grabber. This allowed moving the Ronchi ruling together with data acquisition from a single computer, so

many ronchigrams could be acquired simply by introducing the name of the recorded file and the corresponding positions for the motors, without any further operation from the researcher. The communication routines between both computers were also programmed in C language. A diagram of the connections between computers may also be seen in Fig. 4.1.1.

4.1.5.- Image acquisition equipment

The last step involves recording the ronchigram for further processing. A Pulnix© TM-765 CCD camera with 512x512 pixels was used. It was connected to a Data Translation DT-2853 high resolution frame grabber with two on-board memory buffers, which digitized 8-bit levels. This frame grabber was inserted in the aforementioned 80486 PC. The image captured could be seen in real time on a Zend© Z-1504F RGB monitor connected to the frame grabber. The programs which controlled the camera were written in C language.

Here it was impossible to avoid the inclusion of an objective for the CCD camera, which might distort the wavefront to some extent. However, the measured values obtained in Sections 6 and 7, when compared with measurements performed using other measurement techniques, show that this effect has little importance. The highest quality objective available to us was a Rainbow G50 1:1.8 fixed focal objective with 50mm focal length. The objective was set pointing at infinity, so each pixel on the CCD could be associated with a given direction of the incident light. This fact will be used in Section 4.2 to measure the slopes along the X and Y direction of the wavefront on the Ronchi plane.

The average size of the pixels of the CCD was needed in the measurements of the slope on the Ronchi plane. It was measured through evaluation of the lateral magnification for a distant object ($m = f'/z = y'/y$), by comparing the real size of a distant object with its size in number of pixels, yielding average values for the pixel size of 10.4μm along the X axis and 11.2μm along the Y axis. As this measurement was carried out with the camera in its usual working conditions, it is expected to include to some extent any possible distortion introduced by the objective, the video signal generation in the CCD camera and the signal acquisition by the frame-grabber.

Finally, at least two ronchigrams with the ruling placed in perpendicular directions needed to be registered to start the data processing, which required a more

powerful computer than an 80486 PC. It was thought that a Pentium 150 PC could replace the 80486 PC present in the laboratory, but memory requirements showed that the DT-2853 frame-grabber and the Pentium PC were not compatible. The Pentium PC was thus connected to the 80486 PC via its parallel port, so fast data transfer was enabled, leaving the data acquisition for the 80486 PC and the data processing for the Pentium PC.

4.2.- Data processing

Now the experimental setup has been described, we will present the set of steps that leads from a pair of recorded orthogonal ronchigrams to the final reconstruction of the surface topography, and to measuring its radius of curvature. As in Section 4.1, an initial general overview of the full process will be presented prior to the detailed analysis of each of the steps involved. The whole process is summarized in Fig. 4.2.1. All the data processing operations (except the final curve-fitting procedures) were carried out using software developed by the authors themselves, programmed under a C language outline.

A pair of ronchigrams with the Ronchi ruling lines set in orthogonal directions (in our case, along X and Y axes) are needed in order to obtain the topography of a surface. Each of them is smoothed by convolution with an equienergetic 5x5 matrix, all of whose elements are equal. This step reduces the random noise present in the Ronchigram, and greatly enhances the performance of the threshold process carried out next, where all pixels over 25% of the signal from the ground intensity level are marked as active ones, leaving the remaining ones as inactive pixels. An eroding process is then started in order to reduce each of the ronchigram lines (in the beginning some tenths of pixels wide) to its central line, just one pixel wide. Once this process has been completed for both ronchigrams, the line patterns obtained are superimposed in order to find their intersection points. From each of these intersection points the components of the normal vector to the wavefront at a given point of the Ronchi ruling

Fig.4.2.1: Data processing diagram.

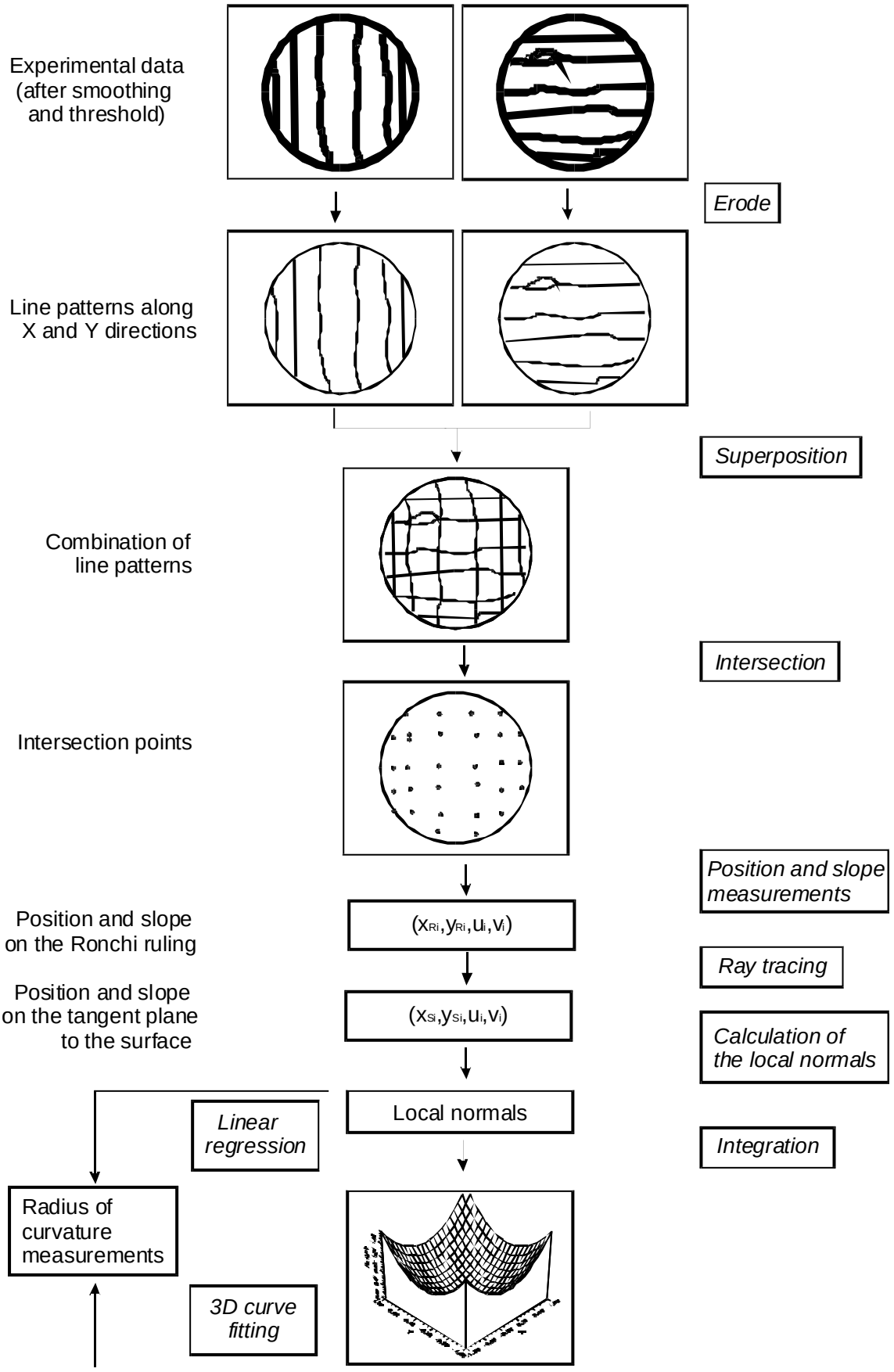
Experimental data (after smoothing and threshold)
Erode
Line patterns along X and Y directions
Superposition
Combination of line patterns
Intersection
Intersection points
Position and slope measurements
Position and slope on the Ronchi ruling
(xRi, yRi, ui, vi)
Ray tracing
Position and slope on the tangent plane to the surface
(xSi, ySi, ui, vi)
Calculation of the local normals
Local normals
Linear regression
Integration
Radius of curvature measurements
3D curve fitting

plane may be obtained. The direction and position of a set of rays impinging on the Ronchi ruling were thus measured.

Through ray-tracing backwards to the surface, the points on the surface where each reflected ray started may be calculated, provided the distance between the Ronchi ruling and the surface is known. As the position of the point source relative to the surface is also known, the slope of the ray incident on the surface may be measured using the known position where the reflected ray starts. Once the direction of the incident and reflected rays are obtained, the normal to the surface at that point on the surface (the local normal to the surface) may be measured through the classic reflection law. When this has been achieved, the surface profile may be obtained through numerical integration of the local normals obtained.

In the cases of spherical and toroidal surfaces, which will be considered in Sections 6 and 7, the parameters of the surface may be measured either via three-dimensional curve-fitting of the surface (carried out using commercial software, TableCurve© 3D) or through linear regression of the component of the local normal against the corresponding position coordinate, which yields the radius of curvature of the surface along the two-dimensional section of the surface selected. This linear regression step has also been attained using commercial software programs (Table Curve© 2D). In the case of toroidal surfaces, this step can be achieved by carrying out the regression along any of the two circular sections present in the toroidal surface.

4.2.1.- Preparation of the ronchigrams

Unavoidable experimental noise is recorded together with the data, which considerably complicates the data processing to be done. In order to reduce the effects of this experimental noise, a smoothing operation is performed. Experimental data is convoluted with a 5x5 equienergetic matrix, all of whose elements are equal. A smoothing step is a common initial operation when working with ronchigrams [Alcalá 94] [González 1987].

This smoothed data is then binarized using a common threshold operation, whose threshold value is fixed at 25% of the signal, once the background noise has been subtracted. This yields a two-level processed ronchigram in which the higher intensity values have been set at the same fixed intensity level. The shadows of the lines in the Ronchi test have thus been transformed into lines some tenths of pixels

wide, without any intensity variation inside these. Transformed experimental measurements closely resemble the starting data of Fig. 4.2.1.

As we are interested in the position of the center of each fringe, smoothing and threshold operations are expected to leave the data to be measured unaltered, or with very minor modifications.

4.2.2.- Eroding the ronchigram

Each of the ronchigrams is then eroded using a software program following the flux diagram presented in Fig. 4.2.2. An iterative procedure is started containing a first step which detects the edges of the lines contained in the ronchigram at that time in the program execution, followed by the eroding process, which is carried out for each of the pixels identified as edges of one line.

At each particular pixel, the eroding procedure considers the value of each of its neighbouring pixels in order to decide whether the elimination of that pixel would introduce a discontinuity in the line or not. If the continuity of the ronchigram line considered is preserved, the pixel may be eroded. The process is repeated over the whole image as many times as required to completely reduce the wide line pattern to a one pixel wide line pattern.

Because of the simplicity of the algorithm considered, sometimes undesired lines orthogonal to the central pixel line appeared. These undesired lines were then removed through an algorithm which detected the line edges and removed any lines shorter than a given preset value.

4.2.3.- Sampling slope and position of the wavefront from a pair of ronchigrams

Our aim is to measure both rotationally and non-rotationally symmetric surfaces. In the latter, a pair of ronchigrams are required in order to properly sample the three-dimensional slope of the wavefront in a set of positions. Whenever rotational symmetry of the surfaces may be assumed, a single ronchigram might provide enough information to yield a full surface reconstruction of the wavefront [Cornejo 1970]. In our work, even in the case of rotationally symmetric surfaces, such as spherical ones, two ronchigrams will be used in order to avoid making assumptions on the measured surface and to keep the measurement method general.

Fig. 4.2.2: Flux diagram of the eroding procedure.

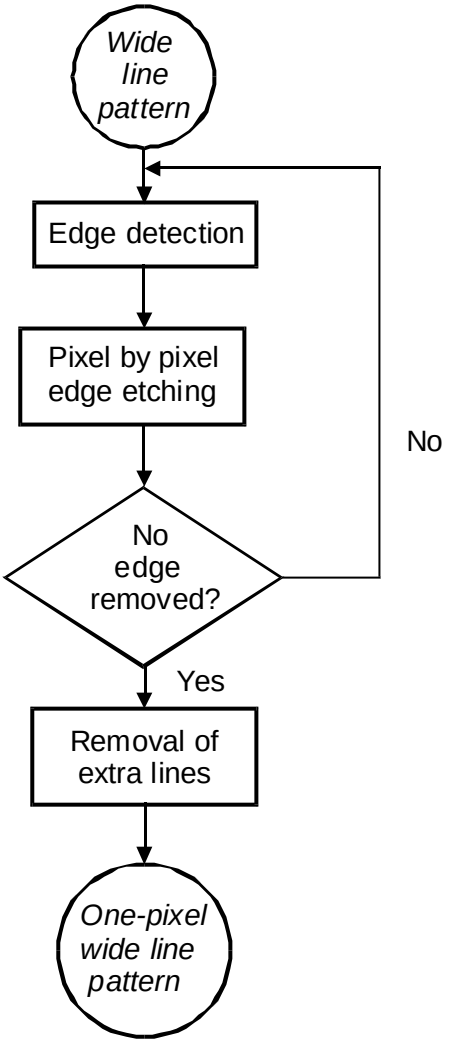

Our goal is to measure the slope of the wavefront at a set of points on the Ronchi ruling. This means that at each sampling point four quantities must be measured: its coordinates on the Ronchi plane (x_R and y_R) and the slope of the wavefront along the X and Y directions (u and v). An origin for the measurement of positions will be provided in the experimental arrangement.

Slope measurements are carried out by making use of the properties of the objective, which has been set pointing at infinity. Fig. 4.2.3 shows the geometry of the experiment, together with the parameters used in slope calculations. In the setup represented in Fig. 4.2.3, obviously, the lines of the Ronchi ruling have been placed along the Y axis, allowing both x_R and u to be measured. Measurements of y_R and v are obtained when the lines on the ruling are placed along the X axis. From Fig. 4.2.3 it may be seen how

Fig. 4.2.3: Measurements of position and slope from the ronchigram.

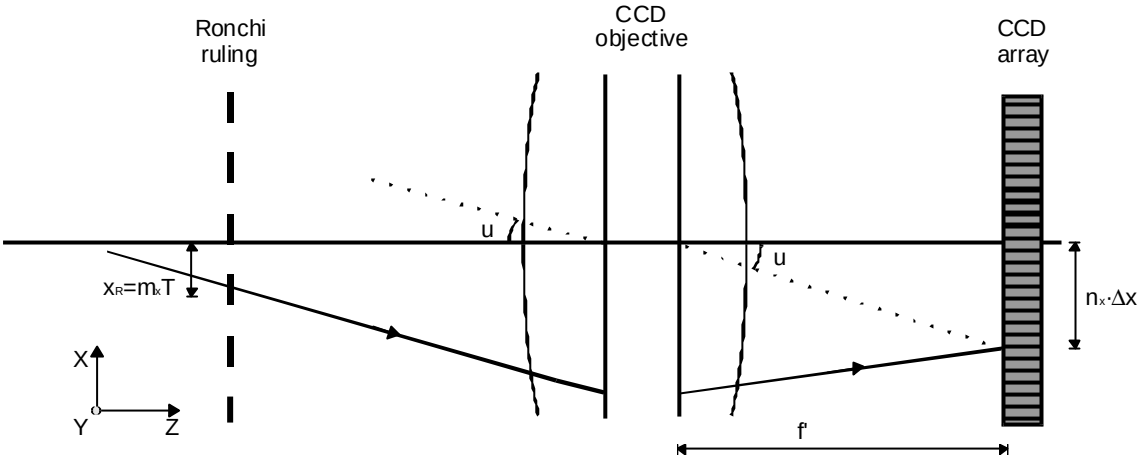

$$u = n_x \cdot \frac{\Delta x}{f'}$$
$$v = n_y \cdot \frac{\Delta y}{f'} \qquad (4.2.1)$$

where Δx (Δy) is the size of the pixel along the X (Y) axis, f' is the focal length and n_x (n_y) the distance of the considered pixel from the central one in number of rows (columns). The origin for the slopes along the X or Y axis is the central row and column of the CCD array.

Position is measured using the shadow pattern recorded onto the CCD array, as consecutive bright (or dark) lines on the ronchigram are one period away from each other. Thus

$$x_R = m_x T$$
$$y_R = m_y T \qquad (4.2.2)$$

where T is the period of the ruling and m_x (m_y) is the distance of the considered fringe from the central one in number of lines. An origin needs to be defined in order to measure the absolute position of one of the lines on the ronchigram, as the position of the remaining lines relative to each other is known through the ruling period. In order to make an absolute measurement for one of the lines, one of the lines in the Ronchi test was “marked”, in order to be distinguished from the others, and its absolute position was measured experimentally. When performing a measurement, the Ronchi test is moved through the motor encoders exactly an integer number of periods in order to take the “marked” line out of the field of view. As the absolute value of the position of the “marked” line is known, and the amount of displacement introduced by the motor

encoders is also known, an absolute value for the position in each of the directions (X and Y) may be determined for each of the lines present in a ronchigram. As an integer number of periods has been moved, a ruling line will be placed exactly where the "marked" line was.

To give an example of this, if we now come back to the one-pixel-wide line pattern which we calculated earlier from the original ronchigram, we see how each of the pixels in the line left active has the same position coordinate (along the axis orthogonal to the direction of the line), but the rays impinging on different pixels of that line have different slopes.

Finally, in order to obtain the required set of four values x_R, y_R, u, v, two ronchigrams with their lines placed orthogonally are superimposed, and their intersection points determined. At each of these intersection points data from both ronchigrams are available, which will complete the values for the position and slope of the wavefront along the X and Y axes at that given point. Improvements to the sampling of the wavefront will be studied along Section 5.

4.2.4.- Measurement of the local normal to the surface

At this point, a set of slopes and positions on the Ronchi plane are known. However, we would like to obtain the information on the tested surface which these contain. In Section 3.3.2, equations for the measurement of the local normal vector to the tested surface were developed, starting from the slope and position values that were measured above. Figure 4.2.4 shows the geometry that was assumed.

Fig. 4.2.4: Geometry and reference systems used in local normal measurements.

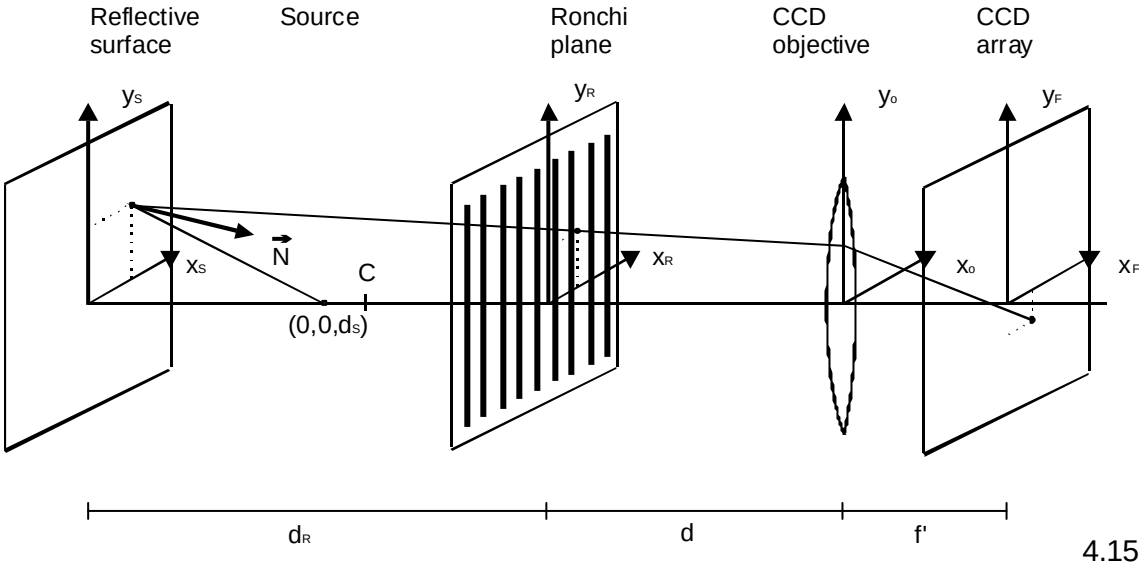

It was shown how, when the points and slopes present in the Ronchi ruling were ray-traced backwards to the plane tangent to the surface at its vertex, a set of points on the surface with known slopes from the reflected ray were found, and described by

$$x_S = x_R - \frac{d_R}{f'}x_f = m_x T - \frac{d_R}{f'}n_x \Delta x$$
$$y_S = y_R - \frac{d_R}{f'}y_f = m_y T - \frac{d_R}{f'}n_y \Delta y \qquad (4.2.3)$$

with d_R being the distance from the Ronchi test to the vertex of the surface, and the remaining parameters defined consistently with those of Section 4.2.3, that is, m_x (m_y) stands for an integer meaning the number of periods of the Ronchi ruling where the considered ray is impinging the ruling along the X_R (Y_R) axis, and n_X (n_Y) is the whole number of pixels from the central row (column) along the X(Y) axis the considered pixel is. When ray-tracing from the Ronchi ruling plane to the surface, each of the intersection points in the superposition of the ronchigrams with orthogonal ruling lines will give a sampling point on the surface .

Light impinging on each of these points on the surface comes from the point laser source. In our experimental setup, the source is placed on the axis at a distance d_S from the vertex of the surface (fig.4.2.4). This allows the slope of the incident ray to be measured, and this, together with the knowledge of the slope of the reflected ray at each sampling point, allows the measurement of the normal to the surface at that point, that is, the local normal to the surface. At each point, it was shown in Section 3.3.3, eq. 3.3.6 how the local normal is equal to

$$N_x = \frac{n_x \Delta x}{2f'}\left[1 + \frac{d_R}{d_S}\right] - \frac{m_x T}{2d_S}$$
$$N_y = \frac{n_y \Delta y}{2f'}\left[1 + \frac{d_R}{d_S}\right] - \frac{m_y T}{2d_S} \qquad (4.2.4)$$

with the source placed at $(0,0,d_S)$

This equation was calculated using two assumptions. First, the wavefront must vary smoothly, so different positions must have different slopes (shadows do not cross each other). Second, the coordinates of the points on the surface are not actually calculated on the real surface, but on the plane tangent to the surface at its vertex, parallel to the $X_R Y_R$ plane. In order to investigate how much the data points were altered when ray-tracing back to the real surface, we used an iterative procedure which, once the topography of the surface was obtained, ray-traced the set of points on the Ronchi ruling onto the calculated surface again, yielding a new set of points on the surface, and

a new reconstructed topography. However, the observed differences in the case of concave surfaces of ophthalmic lenses (with measured sagittas around 0.5mm) were of very little significance, so ray-tracing to the tangent plane could be assumed to be accurate enough in our experimental conditions, where the light source is close to the center of curvature of the surface. This assumption will be further justified along Section 6.2, when performing topographic measurements in spherical samples.

4.2.5.- Surface reconstruction

The only step remaining before the full surface topography is obtained is surface integration. This means calculating the Z coordinate for a set of points on the plane tangent to the surface at its vertex where the slope of the real surface (its local normal) is known. A simple integration algorithm was also developed and programmed.

A flux diagram for the algorithm is presented in Fig. 4.2.5. The algorithm divides the sampled surface into areas centered at each measured sampling point on the tangent plane to the surface, but containing in their surroundings at least four additional measured sampling points. This is achieved by defining a search radius around each sampled point. The slope values for each of the data points are averaged with a weighting factor proportional to the inverse distance to the central data point. This average was set in order to account for any possible duplications of data points that may appear in the intersection procedure (one such point may be seen in Fig. 4.2.1, second row, second column, starting from the top left). If this duplication did not exist, the weighting factor would be strong enough to yield a slope value consisting almost uniquely of the slope of the central point.

One consequence of this approach is that all areas are circular, and that there is a high degree of overlapping between neighboring areas. The number of sampled points in each area need not be constant. Each of the areas will be iteratively raised to a given height until the relative displacement between neighboring areas in the whole tested surface is under a preset value.

At the beginning of the iterative procedure, a group of areas containing one central point and at least four additional points is defined. The slope of the central point is the weighted average previously defined. As each of the points in the area is the central point of some other area, they will also have weighted slope values. For each pair of points inside an area, the height variation is calculated as

Fig.4.2.5.- Flux diagram of the integration algorithm.

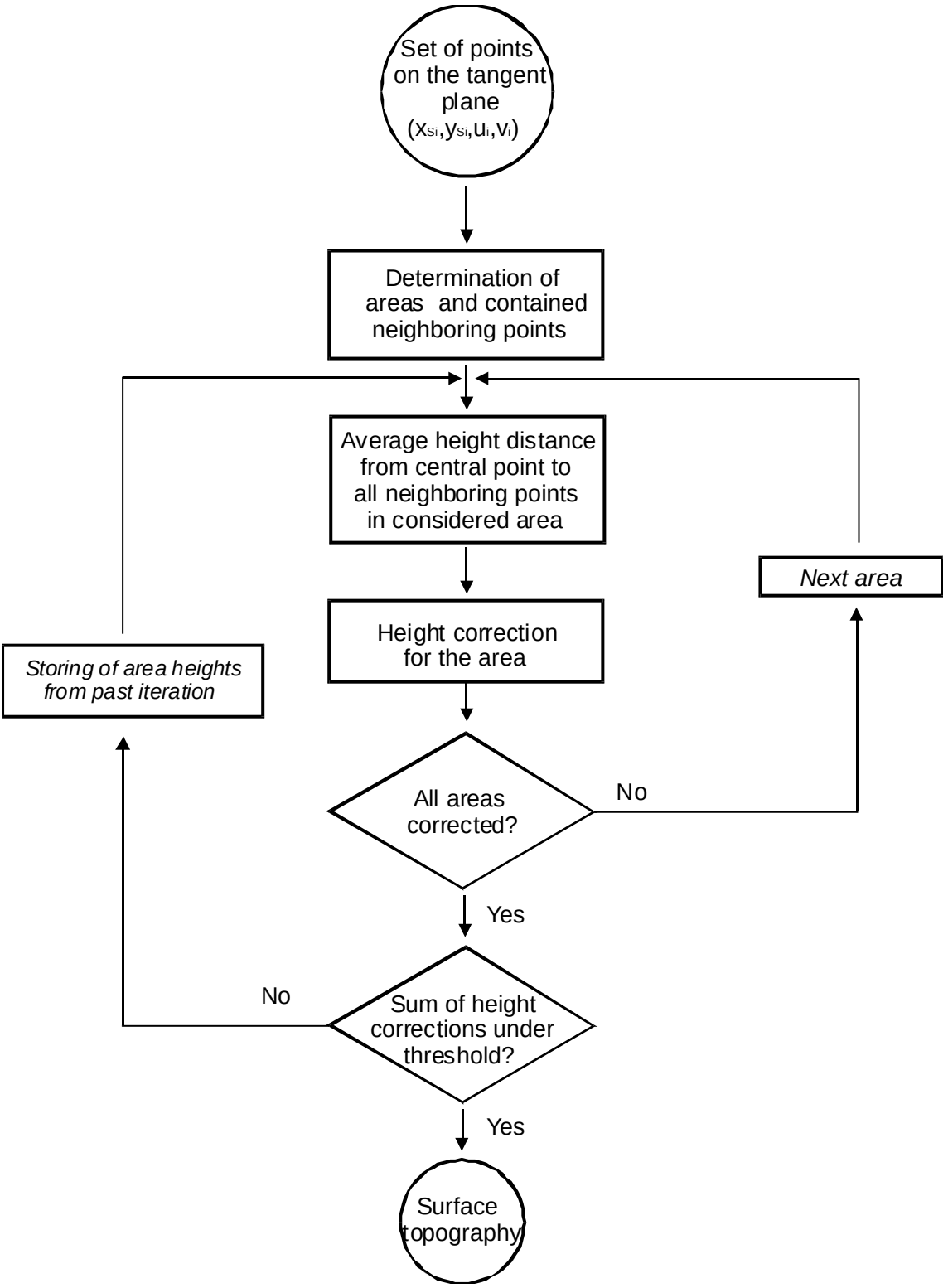

$$\Delta h_{1-2} = \frac{1}{2}\left(\left(\frac{u_1 + u_2}{2}\right) \cdot \Delta x_{1-2} \right) + \frac{1}{2}\left(\left(\frac{v_1 + v_2}{2}\right) \cdot \Delta y_{1-2} \right) \qquad (4.2.5)$$

where N_X and N_Y are the projections of the local normal along the X and Y axis, and Δx_S and Δy_S are the differences of the position coordinates of the pair of points. This height variation is calculated for the central point relative to each of the neighboring points present in its area. The average of the total height variations of all neighboring points related to the central point in the area, calculated with its sign, is the distance that this area will be raised. When a new area is considered, areas that have already been computed are considered with their last calculated height. Once all areas have been moved, the process starts again until the total amount of height displacements in the whole sampled area is under a preset threshold value.

Fig. 4.2.6 shows one area, termed *i*, with its central point and five neighboring points. The height distance from the central point with the remaining five neighboring points is determined through Eq. 4.2.5. Its average value will be the height that this area will be raised. Neighboring point number 2 is actually the center of another area, called *j*, where the central point of area *i* will be a neighboring point. Each of the neighboring points is the center of an area, but only two areas have been drawn in the figure for the sake of clarity.

As this iterative procedure is quite time-consuming, depending on the number of sampling points involved, strategies were developed in order to reduce its calculation time. These strategies involve random selection of the areas to be moved and association of each point with its neighbors, in order to avoid unnecessary re-calculation of the neighboring points in each area at every iterative step. However, calculation time is still around some tenths of a minute in common measurements, such as those presented in Sections 6 and 7, which involve about 10^4 sampling points. However, these experiments are carried out using microstepping techniques, which involve 20 ronchigrams (see Section 5.3). When only two ronchigrams are used in the measurement, the number of sampling points drops to 10^2 and the integration time required involves just a few seconds.

Fig. 4.2.6: i and j neighboring areas. All neighboring points in area *i* are central points of their own area. Only two areas (*i* and *j*) have been drawn.

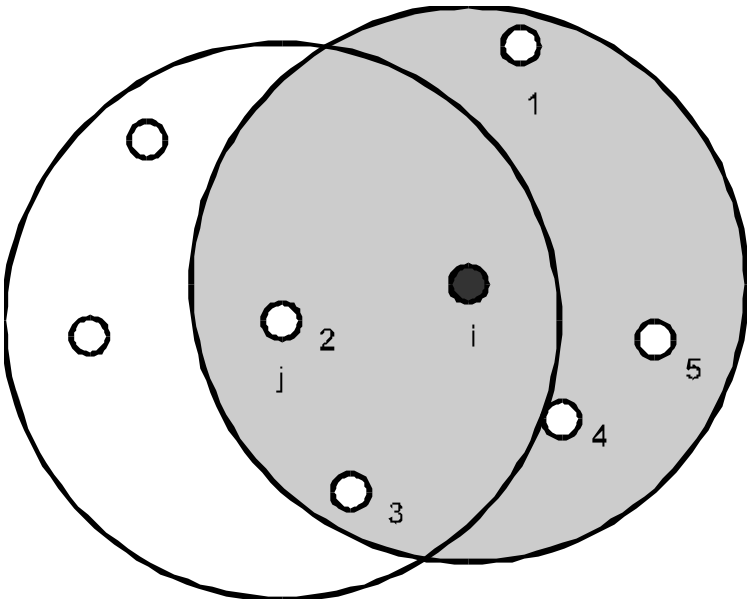

4.2.6.- Characterization of the measured surface

Finally, the surface obtained may be characterized via its most common parameters. This was achieved through two independent procedures. The first one involves using commercial software (TableCurve 3D©) in order to fit the measured surface to an expected surface. Regression coefficients and deviations from the expected data may easily be computed and visualized this way.

However, an alternative procedure was developed in order to measure the characteristic parameters of the surface prior to the integration step. At the point when the local normals to the surface were known at a set of points on the tangent plane to the surface, the set of quantities x_S, y_S, N_X and N_Y were measured. In the case of spherical surfaces, the characteristic parameter we would like to measure is its radius of curvature, whereas in the case of toroidal surfaces two radii placed in orthogonal directions need to be measured.

Along a circular section, the curves $N_x(x_S)$ and $N_y(y_S)$ must be straight lines, with the slope of the line being the inverse of the radius of curvature of the circular section, as may be seen in Fig. 4.2.7. The following small angle approximation is used:

Fig. 4.2.7: Circular section showing relationship between slope, position and radius of curvature.

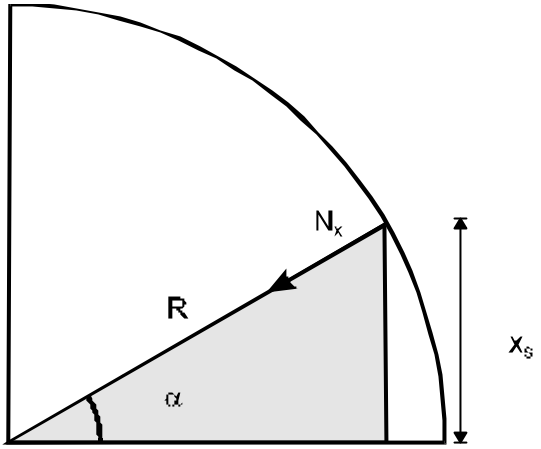

$$N_X \cong \alpha \cong \frac{x_S}{R} \cong C \cdot x_S \qquad (4.2.6)$$

R being the radius of curvature and C the curvature of the surface. Therefore, the linear regression of the $N_X(x_S)$ plot will yield the radius of curvature of the surface as the inverse of the slope of the curve (Fig. 4.2.8). As all sections are circular on a spherical surface, radius measurements are straightforward.

In the case of toroidal surfaces, the plots of $N_X(x_S)$ and $N_Y(y_S)$ will only be linear along the circular sections of the toroidal surface, which provides us with a tool to measure not only its two radii of curvature, but also to estimate the direction in which these radii may be found on the surface. This approach will be further developed in Section 7.

Fig. 4.2.8: Linear regression coefficients yield the surface's radius of curvature.

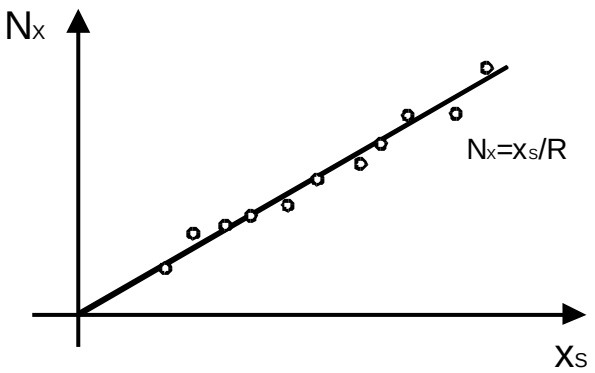

4.3. Accuracy of the measurements

Now the technique, the experimental setup and the data processing involved have been presented, a detailed study of the accuracy of the measurements being made may be carried out. The data obtained in our surface reconstruction technique will be studied in two separate steps. The accuracy of the measurements of the local normal to the surface at each sampling point will first be studied through the local values obtained for the radius of curvature at each sampling point. Once the accuracy of each measurement of the local curvature of the surface is known, the total accuracy obtained when combining all sampled data points to yield a full surface topography will be studied.

4.3.1.- Accuracy of the determination of the local radius of curvature.

As a final result of the point-by-point procedures performed throughout the data processing operations, the direction of the local normal at a point on the tangent plane to the surface is calculated. Not taking into account, as explained in previous sections, very minor effects introduced by the fact that we are ray-tracing to the tangent plane to the surface, and not to the surface itself, two position values (x_S,y_S) and the two components of the local normal along the X and Y axes (N_X,N_Y) may be measured at each sampled point.

Let us define a local radius of curvature for each *i* sampled point, from Fig. 4.2.7a, where it has been shown that

$$N_x^{(i)} = \frac{x_S^{(i)}}{R_x^{(i)}} = C_x^{(i)} x_S^{(i)}$$
$$N_y^{(i)} = \frac{y_S^{(i)}}{R_y^{(i)}} = C_y^{(i)} y_S^{(i)} \qquad (4.3.1)$$

therefore a local value for C_x and C_y may be obtained. $C_x^{(i)}$ and $C_y^{(i)}$ will be termed local curvatures along the X and Y axes at point *i*, placed in position ($x_S^{(i)}$, $y_S^{(i)}$) of the tangent plane to the sample surface. In the case of spherical ($C_x^{(i)}=C_y^{(i)}$) surfaces, or toroidal surfaces with its two orthogonal sections placed along the X and Y axes ($C_x^{(i)}\neq C_y^{(i)}$), all sampled points along a circular section will theoretically have the same local radius of curvature value (under the experimental uncertainty limits), meaning that the curves $N_X(x_S)$ and $N_Y(y_S)$ are straight lines. In toroidal surfaces tilted around the Z axis from the

described position, the value of the local radius of curvature will vary, being constant only along the directions of its two circular sections.

Our goal will be to describe to what accuracy the described technique can measure the local curvature of the surface, taking into account the accuracy of each of the direct measurements involved. This accuracy is almost the same along the X and Y axes, as the only difference between the two directions is a slight variation in the measured pixel angular size, whose respective values are

$$\xi_x = \frac{\Delta x}{f'} = 2.087 \cdot 10^{-4} \text{rad}$$
$$\xi_y = \frac{\Delta y}{f'} = 2.221 \cdot 10^{-4} \text{rad} \qquad (4.3.2)$$

being Δx and Δy the average pixel size along both axes.

From now on, the accuracy in both directions will be considered identical for the sake of simplicity, and only one expression will be written for X and Y directions, containing the X coordinate and subscripts. It must be understood that equations for the Y coordinate may be obtained simply by changing the coordinates and subscripts. The slight difference in the pixel angular size will lead to irrelevant differences between the accuracy in both directions in the final steps of this section, when a numerical estimate for the accuracy of the measurement of local curvature is developed. The superscript (i), referring to the sampling point *i*, will also be removed in order to improve the readability of this section, it being understood that, in all cases in Section 4.3.1, curvatures, positions and slopes will refer to one individual sampling point, that is, these are local values, not general ones calculated for the whole surface.

Following the definitions used in Section 4.2.4, and the geometry, reference and notation described in Fig.4.2.4, it was shown in Eq.4.2.3 that the position of the ray-traced sampled point on the Ronchi ruling onto the tangent plane to the surface equals (Eq.3.3.4)

$$x_S = m_x T - \frac{\Delta x}{f'} n_x d_R = m_x T - n_x x_x d_R \qquad (4.3.3)$$

using the defined pixel angular size. The local normal to the surface was shown to be (Eq. 4.2.4)

$$N_x = \frac{n_x \Delta x}{2f'}\left[1 + \frac{d_R}{d_S}\right] - \frac{m_x T}{2d_S} = \frac{n_x \xi_x}{2}\left[1 + \frac{d_R}{d_S}\right] - \frac{m_x T}{2d_S} \qquad (4.3.4)$$

Through the combination of Eq.4.3.1, 4.3.3 and 4.3.4, an expression for the local curvature may be obtained after some algebra, yielding

$$C_x = \frac{1}{2d_S} + \frac{1}{2d_R}\left[1 - \frac{1}{1 - \frac{n_x x_x}{m_x T} d_R}\right] \qquad (4.3.5)$$

where we remind the reader that d_S is the distance from the source to the surface being tested, d_R the distance from the Ronchi ruling to the surface, n_x the pixel number from the central row at the CCD array, ξ_x the pixel angular size, that is, the pixel size divided by the focal length of the CCD objective, m_x the fringe number and T the period of the Ronchi ruling.

As all the aforementioned parameters are direct measurements carried out in the experimental setup, each with its relative known uncertainty, a conventional error analysis technique through partial derivatives will yield the uncertainty in the indirect measurement of local curvature [Spiridonov 1973]. When absolute values of partial derivatives are taken, it may be shown that

$$\Delta C_x = \frac{1}{2d_S^2}\Delta d_S + \frac{\frac{x_x}{2m_x T}}{\left[1 - \frac{n_x x_x}{m_x T} d_R\right]^2}\Delta n_x + \frac{\frac{n_x}{2m_x T}}{\left[1 - \frac{n_x x_x}{m_x T} d_R\right]^2}\Delta x_x + \frac{\frac{n_x x_x}{2m_x T^2}}{\left[1 - \frac{n_x x_x}{m_x T} d_R\right]^2}\Delta T +$$

$$+\left\{\frac{1}{2d_R^2}\cdot\left[1 - \frac{1}{1 - \frac{n_x x_x}{m_x T} d_R}\right] + \frac{n_x x_x}{2d_R m_x T}\cdot\frac{1}{\left[1 - \frac{n_x x_x}{m_x T} d_R\right]^2}\right\}\Delta d_R$$

(4.3.6)

Notice that no error estimation on m_x has been made, as the line number is assumed to be calculated properly. No uncertainty exists in the consecutive line count.

In order to provide a numerical estimate of the maximum possible uncertainty of the curvature measurements, the following typical values for each measurement and its corresponding uncertainty have been assumed:

n_x=100 pixels	Δn_x=1 pixel
ξ_x=2.15 10^{-4}rad	$\Delta\xi_x$=10^{-6}rad
m_x=5 lines	
T=0.508mm	ΔT=2.5 10^{-3} mm
d_R=200mm	Δd_R=0.1mm

d_S=200mm Δd_S=0.1mm

Notice that the value taken for the pixel angular size is the average of the measured values along the X and Y directions (Eq.4.3.2).

This amounts to a curvature measurement of

$$C_x = 8.61\ 10^{-3} \pm 1.8\ 10^{-4}\ mm^{-1}$$

which, in terms of radius of curvature, amounts to

$$R_x = 116.1 \pm 2.5 mm$$

That is, the relative error comes to be around 2% of the measured value. Table 4.3.1 shows the absolute error introduced by each of the terms and its relative weight in the final uncertainty of the measurement. The most important contribution to the error may be seen to come from the uncertainty in the pixel position determination. The pixel angular size also contributes significantly to the uncertainty of slope measurements, showing the importance of the experimental measurement of angular magnification in common camera working conditions, in order to include possible effects of the frame grabber, the CCD camera or the objective on this parameter. Errors in the measurement of the ruling period also present important contributions to the uncertainty of the experiment. On the other hand, in our experimental setup the positioning of the surface entails very little error in the measurement. This is obviously connected with the uncertainty of each of the parameters measured directly: while the distances may be reliably measured with a 0.05% relative error with the available instruments, the pixel number may only be assumed to be properly measured with a 0.2% relative error.

Table 4.3.1: Absolute and relative contribution to the total error of the uncertainties in each of the directly measured parameters.

Uncertainty	Δn_x	Δx_x	ΔT	Δd_S	Δd_R	**TOTAL**
Absolute error (mm^{-1})	$8.81\ 10^{-5}$	$4.10\ 10^{-5}$	$4.34\ 10^{-5}$	$1.25\ 10^{-6}$	$3.85\ 10^{-6}$	$1.78\ 10^{-4}$
Relative error (%)	49.6	23.1	24.4	0.7	2.2	100

It must be recalled, however, that this 2% is a maximum uncertainty value, which defines a curvature band within which each of our sampled point measurements will lie. This 2% value will be shown to be quite an overestimate when analyzing the experimental results obtained.

4.3.2.- Accuracy of the determination of the surface radius of curvature and surface topography from a set of data points.

The next step involves an overall estimate of the accuracy of the measurement of the surface radius of curvature and surface topography. This will be a statistical step, as it depends on the number of data sampling points involved. Furthermore, Section 5.3 puts forward microstepping techniques which allow the number of sampling points to be increased to 10^4, as compared to the 10^2 data points typical when using the techniques presented until now.

As explained above, radii of curvature measurements of the surface using all the sampled points may be obtained via linear regression of the $N_X(x_S)$ and $N_Y(y_S)$ measured values. The correlation coefficient of the linear fitting will provide us with a value for the quality of the measurement, meaning the closeness of the measured data to the expected (linear) data distribution. The alternative procedure used for obtaining the radii, that is, the curve-fitting of the three-dimensional surface through commercial software, has also been used, providing another correlation coefficient value for all the points in the surface. In this case, however, the fitted values are $z(x_S,y_S)$, that is, height (instead of slope) against position.

Correlation coefficients will provide us with a measurement of the proximity of the experiment to the fitted line or surface. However, we would be more interested in an estimate of the accuracy of the measurement of the radius of curvature, and to what extent this accuracy may be improved when more than just one single data point is considered. In statistical terms, this means that we are interested in the shape of the probability distribution of the measured values [Sachs 1984]. Under our experimental conditions, it has been shown that the experimental error in the determination of the linear coefficient of the linear regression $y=a+bx$, in our case $N_X=C_xx_S+K_x$ is described by [Spiridonov 1973]

$$\Delta C_x = \frac{t_P[N-2]}{\sqrt{N-2}} \sqrt{\frac{\sum_{i=1}^{N}\left[N_x^{(i)}-\overline{N}_x\right]^2 - \frac{\left[\sum_{i=1}^{N} x_S^{(i)}N_x^{(i)} - N\cdot\overline{x}_s\overline{N}_x\right]^2}{\sum_{i=1}^{N}\left[x_S^{(i)}-\overline{x}_s\right]^2}}{\sum_{i=1}^{N}\left[x_S^{(i)}-\overline{x}_s\right]^2}} \qquad (4.3.7)$$

where N is the number of data points, and $t_P[N]$ is the value of the Student's t distribution when N data points are known, and the probability of the measured point to stay in the limits defined by $\overline{C}_x \pm \Delta C_x$ is P.

The conclusions we draw from such an equation are two:

- The quality in the linear regression fitting depends on the inverse of the square root of the number of data points. That is, increasing the number of data sampling points has a direct effect on the accuracy of the measurement. In particular, some technique allowing a two orders of magnitude increase in the number of sampled points would yield one order of magnitude improvement in the accuracy of the measurement of the radius of curvature. The interest of reducing the uncertainty of the measurement through increasing the number of sampled points becomes obvious, and will be the subject of Section 5.
- The accuracy has a direct dependence on the deviation from the measured mean values of the experimental data points, that is, on the standard deviation of the measured data. This means that the error will strongly depend on the experimental data values obtained. Although we are aware that an estimate could be achieved assuming probability distributions for the data involved, we understand that each particular set of data points will yield an error estimate, associated to the standard deviation of the data for each of those parameters. An extensive section assuming given structures for the distribution of sampled data points would be, in our opinion, quite unproductive when numerical error values for each experiment are easily computed. The situation is quite similar to that of the correlation coefficient, another key parameter related to the quality of the fitting, which is easily computed, and hardly estimated.

When the error analysis of our measured data is carried out for a typical measurement, in Sections 6.2 and 7.2, standard deviations of all fitted parameters in two-dimensional and three-dimensional fitting procedures will be presented. In these Sections, it will also be presented an uncertainty value assuming a 0.95 probability for the data to fall within the uncertainty band so defined, in a direct application of eq.4.3.7. However, only standard deviation values for three-dimensional fitting procedures will be presented for all samples, as the presented values in the typical experiment will show these values to provide enough information.

A similar reasoning may be followed when talking of the accuracy of the topography reconstructions achieved. As height calculations are related to the distance between neighboring points, increasing the number of points in the surroundings of each other means reducing the number of height steps in X, Y and Z directions. This means that a better surface reconstruction is obtained as the number of sampling points is increased.

As in the case of the error in curvature values obtained through regression, an estimate of the error involved in the surface measurement could be obtained through assuming error distributions on the sampled points. However, height is obtained as a consequence of an iterative integration procedure, which means that an error estimate of the height variations, starting from the slope measurement error is hard to express analytically. Besides, a numerical estimate for each measurement may be easily calculated from the deviations of the height of each point from the corresponding height on the best fit surface. These residual plots will be widely presented along Sections 6 and 7.

So, as a summary, error estimates in the measurements of curvature and height need assumptions on the probability distributions of errors in slope and position values, and, in addition, are easily computed from experimental data. It has also been shown that increasing the number of sampled points improves the accuracy of the measurements of curvature and the quality of the measured topographies of the surfaces. While in the former the number of points in the linear regression is increased, reducing the uncertainty in slope determination, in the latter the accuracy in the height reconstruction is improved. Next Section will describe some techniques which may be implemented in our experimental setup in order to improve the measurements being carried out.